Photophysics of AgCl doped with [Cl$_5$Ir(N-methylpyrazinium)]$^-$: I. EPR, ENDOR and structural calculations

Photophysics of AgCl doped with [Cl$_5$Ir(N-methylpyrazinium)]$^-$: I. EPR, ENDOR and structural calculations

R S Eachus, Th D Pawlik, R C Baetzold, D A Crosby and W G McDugle

Imaging Materials Division, Eastman Kodak Company, Rochester, NY 14650-2021, USA

Abstract. By applying a combination of multi-frequency electron paramagnetic resonance spectroscopy, electron nuclear double resonance spectroscopy and advanced computational techniques, an understanding of the effects of [Cl$_5$Ir(NMP)]$^-$ complexes on the photophysics of AgCl dispersions is emerging (NMP = N-methylpyrazinium). There is indirect spectroscopic evidence that this dopant is incorporated intact during AgCl precipitation. Calculations predict its substitution for an (Ag$_2$Cl$_7$)$^{5-}$ sub-unit of the host lattice, with the NMP ring rotated 45° with respect to the equatorial chloride ligands. Calculations also show that, in grains with edge lengths $\geqslant 0.05$ μm, the majority of dopant centres will be fully charge compensated by association with four silver ion vacancies. A $(101)(\bar{1}01)(01\bar{1})(0\bar{1}\bar{1})$ geometry is favoured, where the Cl–Ir–(NMP) axis defines z. Photo-EPR experiments suggest a small population of under-compensated {[Cl$_5$Ir(NMP)]$^-$ 3V} centres also exists in most of the dispersions studied. During exposure to actinic light, these dopant centres trap electrons. Since the dopant's LUMO is primarily a π^* NMP orbital, the initial photoproducts are ligand-centred, one-electron donors. Experimental ^{1}H hyperfine data obtained by powder ENDOR spectroscopy for the favoured vacancy geometry of {[Cl$_5$Ir(NMP)]$^{2-}$ 4V} are consistent with the unpaired electron distribution calculated by Hartree–Fock methods. Vacancy binding energies are so large that the over-compensated donor ionizes before the extra vacancy diffuses away.

1. Introduction

Optimum imaging characteristics for many photographic materials are achieved by the addition of impurities to the silver halide microcrystals (or *grains*). Polyvalent transition-metal (TM) ions are frequently used as dopants to limit reciprocity effects, control contrast and reduce recombination inefficiencies (Eachus and Olm 1986, Marchetti and Eachus 1992, Olm and Eachus 1999). These dopants interact with photogenerated electrons and holes. Their effects on point lattice disorder (i.e., the concentrations of free Ag$^+$ interstitials and vacancies) are usually of secondary importance in the photographic process.

The preparation of AgX dispersions in gelatin (photographic *emulsions*) by aqueous precipitation facilitates the incorporation of TM ions into the silver halide grains as hexacoordinate complexes that substitute for (AgX$_6$)$^{5-}$ or larger lattice sub-units. Historically, dopants of practical photographic value were TM complexes with halide ligands, although X$^-$ replacement by H$_2$O has occasionally proved advantageous (Endo and Saikawa 1990). More recent doping protocols exploit the remarkable tolerance exhibited by the covalent AgX lattice for the substitutional inclusion of impurities with substantial lattice mismatch, such as the iron group pseudo-halide complexes [M(CN)$_6$]$^{4-}$ (Bell *et al* 1992). It has been established that

a dopant's carrier-trapping properties are functions of the metal ion, its valence state and the composition and stereochemistry of the ligand shell (Eachus and Olm 1991). Thus, there are opportunities to engineer photographic materials with specific imaging characteristics through substitution in the dopant's coordination sphere.

TM complexes in which one ligand is organic comprise a particularly interesting new class of dopants for silver halides. Photographic evaluations reveal that such complexes can impart improved imaging characteristics to state-of-the-art dispersions (Olm *et al* 1994), but little is known about how they are incorporated into the AgX lattice, or their effects on its photophysics. In this report, the first of a two-part series, we describe a study of silver chloride grains doped with $[Cl_5Ir(NMP)]^-$, a complex containing the cationic N-methylpyrazinium ligand (NMP). Advanced calculations of structure and energy have facilitated EPR spectral analyses, structural assignments and the interpretation of photophysical processes. Preliminary powder ENDOR measurements have also aided the interpretation of EPR data. In the second paper in this series, we will describe more detailed powder ENDOR studies of $[Cl_5Ir(NMP)]^-$-doped AgCl dispersions in which the organic ligand is enriched with ^{13}C and/or selectively proton exchanged with ^2D.

2. Experimental details

2.1. Materials

The dopant was prepared by the reaction of K_3IrCl_6 with excess N-methylpyrazinium iodide in aqueous solution. It precipitated as the salt $(NMP)[Cl_5Ir(NMP)] \cdot 2H_2O$, a green–black solid whose composition was determined by elemental and thermogravimetric analyses and confirmed by NMR spectroscopy. The 300 MHz ^1H NMR spectrum showed distinct resonances from both coordinated NMP and the free NMP^+ counter-ion (upper trace, figure 1). The lower trace in figure 1 is an optical absorption spectrum obtained at 298 K from a 2.18×10^{-4} M aqueous solution of this dopant. The peak at 586 nm (2.12 eV), with a molar extinction coefficient of about 2030 l mol^{-1} cm^{-1}, is assigned as the lowest energy d–π^* metal-to-ligand charge transfer transition, an interpretation consistent with the results of the extended Hückel calculations described in section 3 of this paper and published data for the related nd^6 complexes $[(CN)_5Fe(NMP)]^{2-}$ and $[(NH_3)_5Ru(NMP)]^{2-}$ (Toma and Malin 1973).

Cubic silver chloride grains with edge lengths ranging between 0.05 and 0.38 μm were prepared as dispersions by standard double-jet precipitation techniques (Berry 1977). These cubes were doped with $[Cl_5Ir(NMP)]^-$ at nominal concentrations between 10 and 250 molar parts per million (mppm). The position of the dopant in the AgCl grain was an experimental variable. The largest cubes were made with the dopant homogeneously dispersed throughout the lattice or buried in a band extending from the grain core (0%) to 40% of the grain volume. The 0.05 μm grains were homogeneously doped at nominal concentrations of 25 or 250 mppm. Photo-EPR measurements made on AgCl grains precipitated in the presence of 250 mppm N-methylpyrazinium iodide showed that, if the free NMP cation incorporates into this material during precipitation from aqueous solution, it does not trap photocarriers during exposure to actinic light.

To obtain powders for EPR and ENDOR studies, the gelatin was removed from the dispersions by three washing/centrifugation treatments with deionized water. These powders were washed in acetone, dried in air and stored at 4 °C. This procedure leaves a thin protective layer of the peptizer on the surface of each grain.
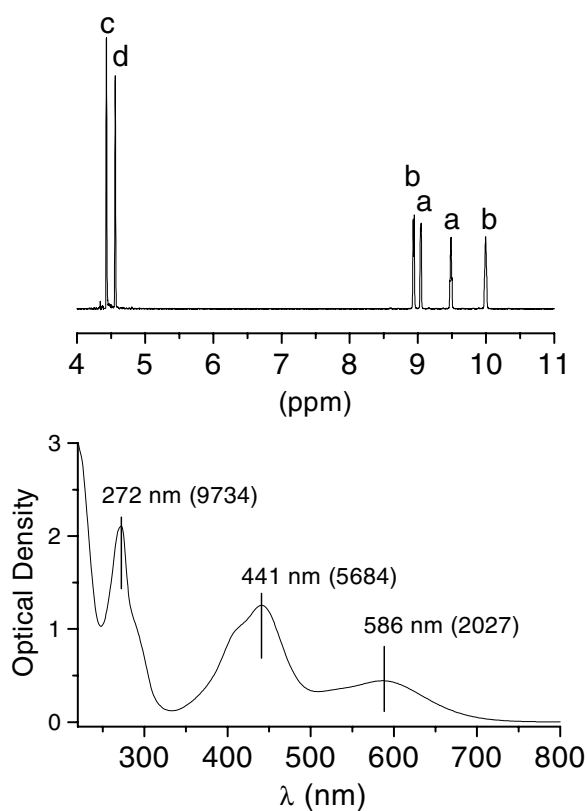
Figure 1. Top: 300 MHz ^{1}H NMR spectrum obtained from a saturated solution of (NMP)[Cl$_5$Ir(NMP)]·2H$_2$O in 2.0 M NaCl in D$_2$O. a = free NMP$^+$ ring protons; b = coordinated NMP ring protons; c = coordinated NMP$^+$ methyl protons; d = free NMP methyl protons. Assignments facilitated by comparison to data obtained from (NMP)I solution in NaCl/D$_2$O. Shifts are relative to the Na salt of TSP. Bottom: optical absorption spectrum obtained at 298 K from a 2.18×10^{-4} M aqueous solution of (NMP)[Cl$_5$Ir(NMP)] · 2H$_2$O. Molar extinction coefficients (l mol^{-1} cm^{-1}) in parentheses.

2.2. EPR and ENDOR measurements

Photo-EPR spectra at 9.3 GHz were measured on a Bruker ESP 300E spectrometer fitted with a helium gas-flow cryostat. *In situ* irradiations were performed with the output of a 200 W super pressure Hg/Xe light source passing through a combination of a 1/8 m monochromator and interference and long pass filters. In these irradiation experiments (section 4), exposures were performed until the yields of photoproducts determined by EPR reached saturation. Thus, it was not necessary to measure the intensity of the exciting light at each wavelength employed. EPR measurements at 35 GHz were made with a Varian E-12 spectrometer fitted with a nitrogen gas-flow cryostat ($T = 82$–298 K). Kinetic measurements were made at 9.3 GHz on the Varian E-12 spectrometer fitted with a helium gas-flow cryostat using an isochronal thermal pulse technique. ENDOR measurements were performed on a highly modified Bruker ER200D X-band spectrometer fitted with a TM$_{110}$ mode cavity and helium gas-flow cryostat. Optimum parameters for the ENDOR experiments were a sample temperature of 8–10 K, a microwave power of 2.5 mW and an RF attenuation of −4 dB. The RF field was either amplitude (AM) or frequency (FM) modulated with a modulation frequency of 2 kHz and a modulation depth of

100% (AM) or 350 kHz (FM). For ENDOR studies, the degelled dispersions were irradiated with band gap light (365 nm) in a nitrogen gas-flow cryostat at temperatures between 82 and 210 K. These samples were then transferred via a liquid nitrogen Dewar into the ENDOR cavity without significant warm-up. The program EPR-FOR (McGavin *et al* 1993) was used to simulate powder ENDOR spectra.

2.3. Computational techniques

The modelling strategies employed in this study comprised a combination of quantum mechanical and atomistic methods. The atomistic technique employed the General Utilities Lattice Programme (Gale 1997) and was used to determine the positions and binding energies of neighbouring compensating silver ion vacancies. This technique has already been described for several dopants (Baetzold 1997, Eachus *et al* 1999). Interatomic classical potentials representing the interactions of dopant ligands with silver and chloride ions were first computed. Then Mulliken charges derived from a Hartree–Fock calculation of the dopant within a point ion lattice were used to specify the net charges on each ion in the dopant complex. The well known AgCl interatomic potentials were used to specify the crystal interactions. In this calculation, the lattice ions were allowed to relax with various adjacent placements of vacancies, while the geometry of the dopant complex was fixed at positions determined in the quantum mechanical calculation. The final state represents the minimum energy of the system, and the lowest energy state for each of the associated vacancies represents the preferred geometry. The difference in energy between this optimum structure and the reference geometry (in which all of the vacancies are separated from the dopant) gives the total vacancy binding energy. Using these binding energies with experimentally parameterized models of the space charge in finite one-dimensional representations, we were able to predict the predominant vacancy-associated species in the AgCl:$[Cl_5Ir(NMP)]^{-/2-}$ system. Details of these latter calculations are beyond the scope of this paper and will be reported separately (Baetzold 2000).

Electron trap depths and spin populations for the dopant in AgCl were calculated by Hartree–Fock methods. The crystal was represented by a spherical array of point charges with surface charges adjusted to give a neutral entity. Appropriate point charges were then removed from the system to be replaced by the dopant complex and any desired vacancies. Born–Mayer potential functions operate between the dopant and its adjacent point ions. This function is described in the appendix and has been employed and parametrized in prior work (Baetzold 1997, Eachus *et al* 1999). The energy of the entire unit was computed quantum mechanically and the dopant geometry was optimized. We employed the CADPAC computer code (Amos *et al* 1995) for this purpose. As many as 20 cycles were required to yield an energy minimum for each dopant–vacancy complex. To compute its electron affinity, the total energy of the dopant at its optimized geometry with and without a trapped electron were compared. In order to obtain the total electron affinity, this first estimate was corrected by the lattice polarization energy determined in an atomistic calculation. This latter type of calculation has been discussed (Baetzold 1997, Eachus *et al* 1999). To obtain trap depths, electron affinities were compared with 3.6 eV, the electron affinity calculated for the AgCl crystal. The electron and spin distributions for the trapped electron state were calculated from a Mulliken analysis of the ROHF wavefunction. This doublet state has one singly occupied orbital. We have found this procedure, as well as UHF/density functional treatments, to yield qualitatively correct spin densities in previous studies of TM complexes in AgCl (Eachus *et al* 1999).

In parts of this paper, we have presented our results in an orbital energy diagram format because this is a familiar chemical construct and aids in understanding the photophysics of the

system. Of course, the unoccupied orbital energies determined in a Hartree–Fock calculation do not have the meaning of a one-electron orbital. The lowest unoccupied molecular orbital (LUMO) was positioned relative to the conduction band edge from the calculated electron affinity.

3. Dopant structure

Structural simulations revealed that a stable substitutional geometry can be achieved for [Cl$_5$Ir(NMP)]$^-$ in AgCl when this dopant replaces an $(Ag_2Cl_7)^{5-}$ sub-unit of the host lattice. Ir occupies an Ag site at the origin. For charge neutrality, four silver ion vacancies (= V) must be created for each iridium complex incorporated. These may be physically associated with the dopant or located at distant sites, with the distribution depending on their binding energies and the lattice temperature. Table 1 includes total binding energies calculated for several geometries of [Cl$_5$Ir(NMP)]$^-$ with two, three or four associated vacancies. For convenience, these structures are labelled Ir 2V, Ir 3V and Ir 4V, respectively. Only the result for the optimal geometry of Ir 2V is included in this table. More comprehensive data for Ir 3V and Ir 4V are shown because they will be used later in attempts to assign EPR spectra. We estimate that differences in the total binding energies $\geqslant 0.2$ eV are significant, given the limits of the approximations inherent in our calculations. Thus, there are two candidates for the most stable geometry of Ir 3V—$(101)(\bar{1}01)(01\bar{1})$ and $(101)(\bar{1}01)(011)$—and three for the most stable geometry of Ir 4V—$(101)(\bar{1}01)(01\bar{1})(0\bar{1}\bar{1})$, $(101)(\bar{1}01)(011)(0\bar{1}1)$ and $(101)(\bar{1}01)(110)(\bar{1}\bar{1}0)$. The model for Ir 4V in AgCl with vacancies at (101), $(\bar{1}01)$, $(01\bar{1})$ and $(0\bar{1}\bar{1})$ is sketched in figure 2. From comparisons of calculations and experiments, we will later argue that this is the preferred structure for the fully compensated centre in AgCl grains.
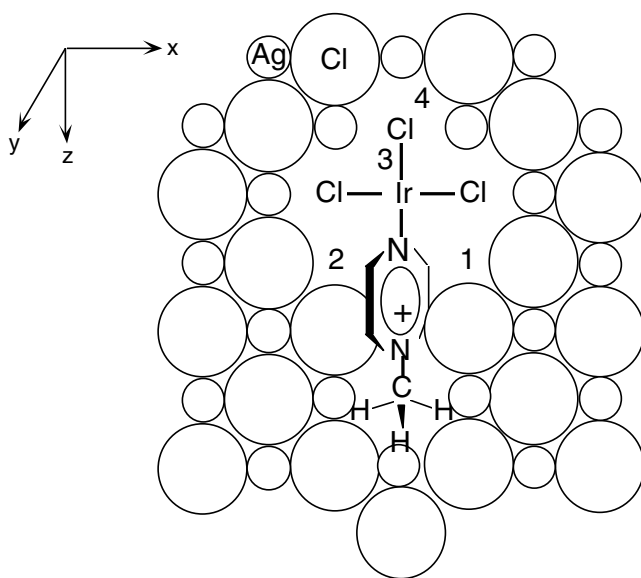

Figure 2. Model calculated for the $(101)(\bar{1}01)(01\bar{1})(0\bar{1}\bar{1})$ geometry of the [Cl$_5$Ir(NMP)]$^-$ centre with four bound vacancies. The dopant substitutes for $(Ag_2Cl_7)^{5-}$. The Cl$^-$ ligands coordinated to Ir above and below the plane are omitted for clarity. The NMP ligand is rotated 45° out of the plane. Sites for the bound vacancies are marked 1–4, with position 3 above the plane and position 4 below the plane.

Table 1. Total vacancy binding energies ($\sum$ BE) calculated for $\{[Cl_5Ir(NMP)]^- nV\}^{(4-n)+}$ centres with various geometries in AgCl.

Dopant complex	Vacancy geometry[a]	$\sum$ BE (eV)
$\{Ir\ 2V\}^{2+} = \{[Cl_5Ir(NMP)]^-\ 2V\}^{2+b}$	$(101)(\bar{1}01)$	3.5
$\{Ir\ 3V\}^{1+} = \{[Cl_5Ir(NMP)]^-\ 3V\}^{1+}$	$(101)(\bar{1}01)(01\bar{1})$	4.4
	$(101)(\bar{1}01)(011)$	4.3
	$(101)(\bar{1}01)(013)$	4.1
	$(101)(01\bar{1})(0\bar{1}\bar{1})$	3.8
	$(101)(013)(0\bar{1}3)$	3.4
	$(10\bar{1})(\bar{1}0\bar{1})(013)$	3.3
	$(10\bar{1})(013)(0\bar{1}3)$	3.1
	$(10\bar{1})(\bar{1}0\bar{1})(01\bar{1})$	2.8
	$(101)(110)(\bar{1}\bar{1}0)$	2.0
$\{Ir\ 4V\}^0 = \{[Cl_5Ir(NMP)]^-\ 4V\}^0$	$(101)(\bar{1}01)(01\bar{1})(0\bar{1}\bar{1})$	5.2
	$(101)(\bar{1}01)(011)(0\bar{1}1)$	5.2
	$(101)(\bar{1}01)(110)(\bar{1}\bar{1}0)$	5.0
	$(101)(\bar{1}01)(013)(0\bar{1}3)$	4.7
	$(110)(\bar{1}\bar{1}0)(1\bar{1}0)(\bar{1}10)$	4.5
	$(200)(\bar{2}00)(020)(0\bar{2}0)$	3.1
	$(10\bar{1})(\bar{1}0\bar{1})(01\bar{1})(0\bar{1}\bar{1})$	2.6

[a] Positions are defined relative to the origin where Ir occupies a silver ion site.
[b] The outermost superscript refers to the effective site charge.

Based upon the data in table 1, it was possible to calculate the dopant's distribution among centres with zero to four bound vacancies as functions of concentration, placement, lattice temperature and grain size. At 298 K, we estimate that about 97% of the centres are fully compensated (= Ir 4V) in 0.05 μm grains doped homogeneously at 250 mppm, the remaining 3% being Ir 3V centres. High dopant concentrations or large vacancy binding energies mitigate the effects of grain size and placement on site populations. Accordingly, the distribution between Ir 4V and Ir 3V centres is only slightly affected by increased grain edge lengths and placements near to the grain's core. For example, in 0.38 μm AgCl cubes doped at 250 mppm from 0 to 40% of the grain volume, over 99% of the $[Cl_5Ir(NMP)]^-$ centres will be fully compensated at 298 K.

The electronic properties of $[Cl_5Ir(NMP)]^-$ in AgCl have been addressed using a combination of Hartree–Fock SCF/ROHF and extended Huckel (EH) methods. Representative results are summarized in figure 3 for the $(101)(\bar{1}01)(01\bar{1})$ geometry of Ir 3V and the related $(101)(\bar{1}01)(01\bar{1})(0\bar{1}\bar{1})$ geometry of Ir 4V. In both cases, the dopant's LUMO level is a π^* orbital from the organic ligand. Calculation by EH methods gives a value of about 2.2 eV for the HOMO–LUMO separation in the AgCl lattice, in good agreement with the value of 2.12 eV derived for the first MLCT transition from the solution spectrum in figure 1. The LUMO levels of these Ir 4V and Ir 3V complexes are placed by SCF/ROHF calculation at 0.26 and 0.55 eV below the conduction band edge of AgCl, respectively. The shift to a deeper electron trapping state as the number of bound vacancies decreases is consistent with arguments based upon the increasing effective site charge. The dopant's HOMO levels lie above the valence band edge for both structures, presenting the possibility of amphoteric trapping behaviour under appropriate conditions.
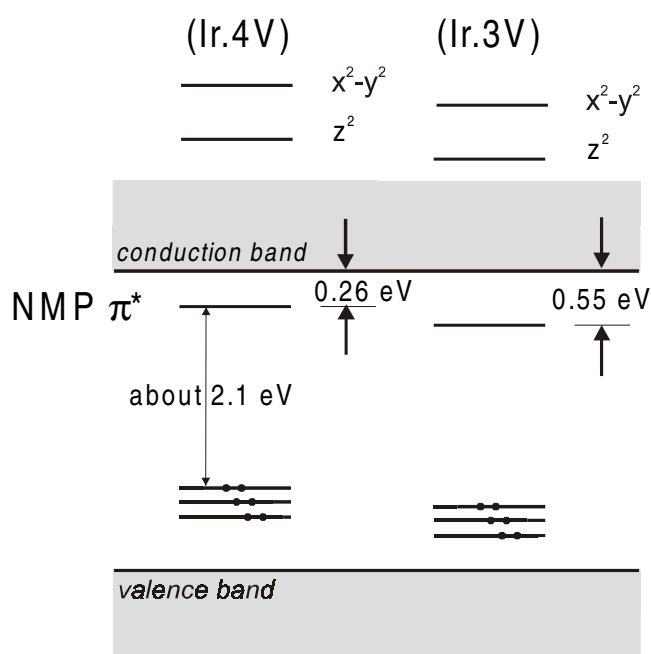
Figure 3. One-electron energy level models calculated for $[Cl_5Ir(NMP)]^-$ centres in AgCl with three (Ir 3V) and four (Ir 4V) bound vacancies. The vacancy geometries in these examples are $(101)(\bar{1}01)(01\bar{1})$ and $(101)(\bar{1}01)(01\bar{1})(0\bar{1}\bar{1})$, respectively.

4. Results and discussion

4.1. Photo-EPR experiments

4.1.1. At T = 10 K. AgCl has an indirect absorption edge that is strongly temperature dependent (Moser and Ahrenkiel 1977). At $T \leqslant 20$ K, the pure material does not absorb radiation in the region 1.55 eV (800 nm) to 3.18 eV (390 nm), and between 10 and 80 K, photophysical processes caused by the absorption of band gap light are dominated by recombination events. Thus, to determine the effect of $[Cl_5Ir(NMP)]^-$ doping on the absorption characteristics and photophysics of AgCl dispersions, EPR experiments began with an assessment of their sensitivity to 400–700 nm (3.1–1.77 eV) excitation at low temperatures. At 10 K, the degelled materials gave no dopant-related EPR signals prior to irradiation, and no signals were observed following excitation at wavelengths longer than 480 nm, i.e., irradiation in the region of the dopant's lowest energy MLCT transition (586 nm) did not result in a detectable valence state change.

First indications of the dopant's photoactivity were detected following exposures to light in the region 440–420 nm. A typical X-band (9.3 GHz) EPR spectrum, obtained at 10 K after 420 nm irradiation at this temperature, is shown in figure 4(a). The sample was a 0.35 μm cubic AgCl dispersion doped homogeneously from 0 to 40% of the grain volume with 250 mppm $[Cl_5Ir(NMP)]^-$. Similar spectra were obtained from cubic AgCl dispersions with edge lengths ranging between 0.05 and 0.38 μm, and doped at nominal levels between 25 and 250 mppm. For equivalent doping levels, the spectrum at saturation was most intense for the smallest grains in this series. There are EPR signals from two species in figure 4(a), one being easily identified from the literature (Höhne and Stasiw 1968a, b) as the self-trapped hole (STH, or
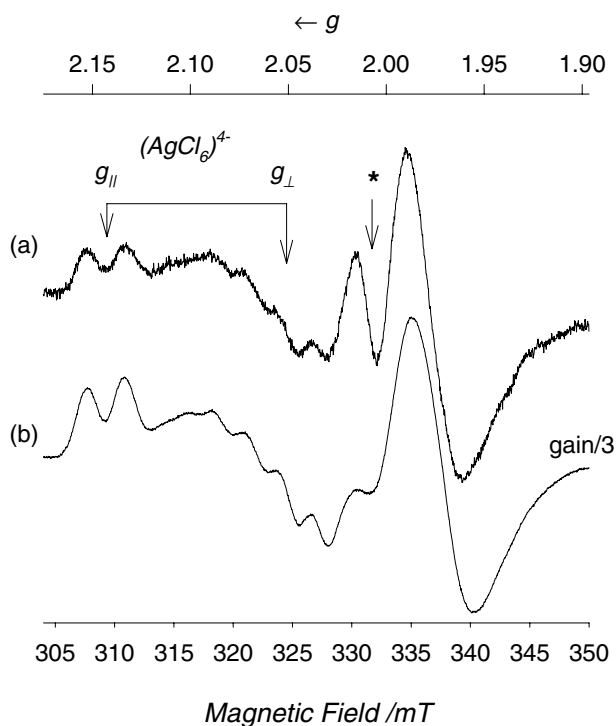
Figure 4. EPR spectra measured at 9.3 GHz and 10 K from a 0.35 μm cubic AgCl dispersion doped between 0 and 40% with $[Cl_5Ir(NMP)]^-$. (a) following 420 nm exposure at 10 K; (b) following 365 nm exposure at 10 K. Note changes in gain between spectra. Signal marked with asterisk in (a) is from a Cu^{2+} impurity in the residual gelatin.

$(AgCl_6)^{4-}$). The second signal, positioned at higher magnetic field, has not been reported previously. It could be satisfactorily simulated assuming a centre of uniaxial symmetry with $g_\perp = 1.978 \pm 0.005$ ($\Delta B_{pp} = 3.5$ mT) and $g_\parallel = 1.953 \pm 0.005$ ($\Delta B_{pp} = 2.8$ mT). With an averaged g factor of about 1.97, and the concomitant detection of self-trapped holes following irradiation, an assignment to a trapped electron centre is justified. However, little structural information can be derived from this featureless signal.

We can rule out an assignment to electrons trapped at shallow ionized donors, since EPR spectra obtained at 10 K from such centres in AgCl invariably consist of single, narrow, isotropic lines centred at $g = 1.880 \pm 0.002$ (Eachus *et al* 1978, Bennebroek *et al* 1995, 1996). Such spectra are basically insensitive to the composition of the trapping defect because, by its nature, a shallowly trapped electron has the magnetic properties of a carrier at the conduction band edge. The central cell correction to the g factor is usually small (i.e., $\leqslant 0.002$), so that a shift of about 0.09 is improbable. We conclude that the signal at $g = 1.97$ in figure 4(a) must originate from an extrinsic deep donor centre. The obvious candidate is $[Cl_5Ir(NMP)]^{2-}$, although the absence of $^{191/193}Ir$ hyperfine (HF) or $^{35/37}Cl$, ^{14}N and ^1H superhyperfine (SHF) splittings makes it difficult to confirm this assignment. Of particular concern is that the dopant could decompose during precipitation, so that the donor spectrum in figure 4(a) results from electron trapping at a byproduct of this process. The most likely decomposition products are $[Cl_5Ir(H_2O)]^{2-}$, $(IrCl_6)^{3-}$ and NMP^+. We can rule out the heterocyclic cation because, as reported in section 2.1, doping with $(NMP)^+$ salts does not introduce photoactive centres into

AgCl dispersions. On the other hand, both [Cl$_5$Ir(H$_2$O)]$^{2-}$ and (IrCl$_6$)$^{3-}$ have high solubilities in this material, where they are known to function as deep electron traps (Eachus and Graves 1976, Eachus and Olm 1991). The resultant donors are metal centred, i.e., the semi-occupied orbitals are primarily 5d$_{z^2}$ on iridium. Consequently, their EPR spectra show well resolved $^{191/193}$Ir HF and $^{35/37}$Cl SHF structure and their *g* matrices are highly anisotropic. In these respects, their EPR spectra are distinctly different from that shown in figure 4(a). From these considerations, and anticipating the preliminary ENDOR results described in section 4.2, we assign figure 4(a) to [Cl$_5$Ir(NMP)]$^{2-}$. This spectrum can best be understood if the trapped electron is confined primarily to the organic ligand so that the small spin density on the Cl$_5$Ir–moiety causes only slight *g* shifts (from 2.0023) through iridium and chlorine spin–orbit interactions. Any ligand SHF splittings are small and buried in the linewidth.

A spectrum similar to that in figure 4(a) was obtained when irradiation was performed with above-band-gap light ($\lambda \leqslant 390$ nm), although the saturation yields of both the STH and the [Cl$_5$Ir(NMP)]$^{2-}$ donor were three to four times larger than those obtained with $\lambda = 420$–440 nm. This is illustrated by comparison of figures 4(a) and 4(b). The signal produced by $\lambda \leqslant 390$ nm excitation could be simulated with $g_\perp = 1.974 \pm 0.002$ ($\Delta B_{pp} = 3.6$ mT), $g_\parallel = 1.945 \pm 0.005$ ($\Delta B_{pp} = 5.5$ mT). There are two possible explanations for the small *g* shifts and linewidth changes with excitation wavelength. The first assumes that the doped AgCl dispersions contain only fully compensated {[Cl$_5$Ir(NMP)]$^-$ 4V}^{0} centres† (= Ir˙ 4V), and that Ir˙ 4V‡ is the only donor produced by both sub-band-gap light and band-to-band excitation. In the case of sub-band-gap light, an electron transfer from the frontier orbital of a neighbouring silver ion (i.e., the perturbed valence band edge adjacent to the dopant) produces this donor and its corresponding acceptor as a spatially correlated pair. Their association causes small shifts in *g* factors from those characteristic of the well separated Ir˙ 4V and (AgCl$_6$)$^{4-}$ centres produced by above-band-gap light. With this model, continuous irradiation with 420 nm light would yield a saturation concentration of Ir˙ 4V/STH pairs equal to that of the isolated Ir˙ 4V and STH centres produced by continuous exposure at 365 nm. This prediction is inconsistent with experiment.

The more plausible explanation assumes that figure 4(b) is a convolution of signals from a multiple population of centres discriminated by the number of bound silver ion vacancies. It consists of a strong EPR signal from Ir˙ 4V centres overlapping a weaker spectrum from {[Cl$_5$Ir(NMP)]$^{2-}$ 3V}^{0} (= Ir˙ 3V). By contrast, irradiation with sub-band-gap light ($\lambda = 420$–440 nm) produces only Ir˙ 3V, the donor contributing to figure 4(a). The implied distribution of the [Cl$_5$Ir(NMP)]$^-$ anion between Ir 4V and Ir 3V centres is consistent with the calculations described in section 3. The difference in the excitation profiles for the generation of Ir˙ 4V and Ir˙ 3V is predicted by the energy level scheme in figure 3. The sensitivity to 420–440 nm light can be attributed to a direct electron transfer transition from the perturbed valence band edge in the vicinity of the dopant to the lowest lying unoccupied mid-gap level, the π^* orbital of the minority Ir 3V centre. A similar model successfully predicted the long wavelength sensitivity imparted to AgCl by doping with (RhCl$_6$)$^{3-}$ (Eachus and Graves 1974). Band-to-band excitation ($\lambda \leqslant 390$ nm), on the other hand, produces excitons and free carriers. Subsequent extrinsic deep electron trapping from the conduction band edge generates Ir˙ 4V and a smaller amount of Ir˙ 3V. We make the reasonable assumption that the *g* matrix of [Cl$_5$Ir(NMP)]$^{2-}$ has a small dependence on the degree of vacancy compensation, so that the shape of the EPR spectrum obtained from a mixture of Ir˙ 4V and Ir˙ 3V donor centres varies only slightly as the excitation wavelength, and thus their relative concentrations, change.

† The superscripts outside the curly brackets refer to effective site charges and are only included in the text where necessary to clarify discussions.
‡ The symbol ˙ indicates an electron trapped at the dopant centre.

Table 2. Representative total vacancy binding energies[a] ($\sum$ BE) calculated for $[Cl_5Ir(NMP)]^{2-}$ centres in AgCl. These results illustrate the tendency for the donor to be over-compensated by silver ion vacancies.

Dopant complex	Vacancy geometry	Σ BE (eV)
$\{Ir^{\cdot}\ 3V\}^0 = \{[Cl_5Ir(NMP)]^{2-}\ 3V\}^{0\ b}$	$(101)(\bar{1}01)(01\bar{1})$	2.91
$\{Ir^{\cdot}\ 4V\}^- = \{[Cl_5Ir(NMP)]^{2-}\ 4V\}^-$	$(101)(\bar{1}01)(01\bar{1})(0\bar{1}\bar{1})$	3.45

[a] Referenced to the charge distribution in the dopant with vacancies present.
[b] The outermost superscript refers to the effective site charge.

4.1.2. At 10 K < T < 220 K.   When samples of $[Cl_5Ir(NMP)]^-$-doped AgCl dispersions were exposed to 365 nm light at 10 K and subsequently annealed in the dark, substantial changes occurred in their EPR spectra. (In the following experiments, spectra were recorded after recooling the annealed material in the dark to 10 K.) For dispersions in which the dopant was incorporated close to the grain surface, and especially for grains with very large surface-to-volume ratios, the internal STH centre began to diffuse between 40 and 50 K. Thermally initiated diffusion of the STH in this temperature range is well documented (Paul *et al* 1987). The experimental manifestation of this mobility was a substantial broadening of its EPR spectrum. This broadened spectrum is assigned to Ag^{2+} ions trapped temporarily at grain surfaces, a conclusion based on the detection of the characteristic $^{107/109}$Ag HF doublet at $g_{\parallel}$, and supported by the analysis of matrix-ENDOR data in section 4.2. Concurrent with the diffusion of the STH, the iridium donor spectrum narrowed slightly. In larger grains, or in dispersions in which the dopant was buried deeply, a substantial population of internal STHs survived above 100 K. At about 120 K, the surface Ag^{2+} acceptors decayed to give a third paramagnetic centre assigned as $(gel)^+$, i.e., a hole trapped off the grain in the residual gelatin peptizer. This product will be discussed in a future report. The $(gel)^+$ radical gave a single, symmetric EPR line at $g = 2.0056$ ($\Delta B_{pp} = 2.0$ mT) and was stable for several minutes at 298 K.

Annealing between 100 and 120 K caused additional subtle, but irreversible changes in g factors and linewidth for the donor signal. This is the temperature region where vacancies begin to diffuse in AgCl, and so, at first sight, one might attribute these changes to ionic relaxation involving the diffusion away of the extra vacancy from the over-compensated $\{Ir^{\cdot}\ 4V\}^-$ donor. However, calculations of vacancy binding energies for related geometries of $Ir^{\cdot}$ 3V and $Ir^{\cdot}$ 4V showed a surprising tendency for the fourth vacancy to remain correlated with the donor centre. The representative data in table 2 show that overcompensation can be favoured by as much as 0.54 eV over the situation in which $Ir^{\cdot}$ 3V and the fourth vacancy are well separated in the lattice. Further annealing up to about 250 K did not effect additional changes in the donor spectrum before it was destroyed by ionization to the conduction band edge. We conclude that the primary donor detected by EPR following band gap exposures between 10 and 250 K is $Ir^{\cdot}$ 4V, and suggest that the slight changes in its g factors and linewidth occurring during annealing are the result of subtle lattice relaxations. For example, a slight rotation of the NMP ring is expected following electron trapping on this ligand. This will cause a concomitant movement of the neighbouring Ag and Cl ions in response to the new charge distribution in the dopant.

A Q-band (35.3 GHz) spectrum obtained at 85 K (figure 5) following 365 nm irradiation provided little additional structural information. Within the limits of spectral resolution at this frequency, the dominant $Ir^{\cdot}$ 4V centre appeared to have uniaxial symmetry. At 85 K, the principal values of its g matrix obtained by simulation are $g_{\perp} = 1.9785 \pm 0.0005$ and $g_{\parallel} = 1.951 \pm 0.001$. Since the trapped electron is confined to the organic ligand, the parallel
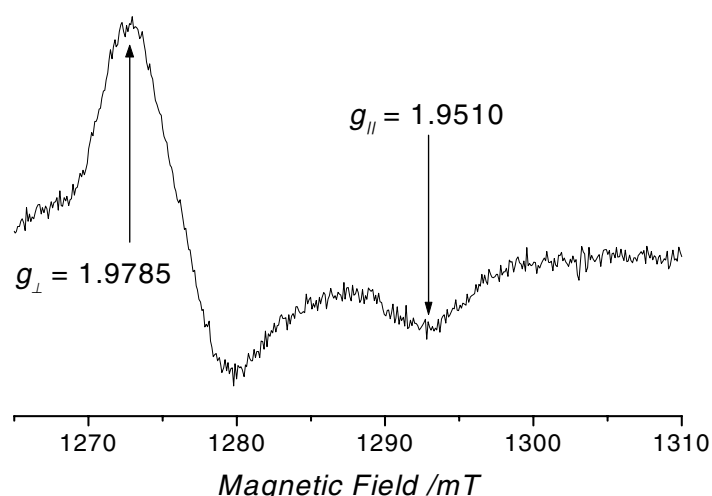
Figure 5. EPR spectrum measured at 35.3 GHz and 85 K from a 0.35 μm cubic AgCl dispersion doped with [Cl₅Ir(NMP)]⁻ following 365 nm exposure at 85 K.

direction of the g matrix is assumed to be normal to the NMP ring plane. From simple theory, when B_0 is aligned along this direction there will be a spin–orbit contribution to the g factor, causing the largest negative shift from the free electron value (2.0023). The g matrix should have rhombic symmetry, but the difference between g_x and g_y must be so small that it is obscured by the spectral linewidths at both X and Q bands.

4.2. ENDOR results and analyses

Figure 6 shows powder ENDOR spectra obtained from a [Cl₅Ir(NMP)]⁻-doped AgCl dispersion following 365 nm irradiation at about 85 K. The grain size was 0.35 μm and the dopant concentration was 250 mppm, parameters chosen to minimize the concentration of Ir˙ 3V centres. These ENDOR spectra were obtained at 9 K, with $B_0 = 342$ mT and using AM modulation. At 9.2 GHz, the field value of 342 mT lies in the centre of the spectrum assigned to Ir˙ 4V. A characteristic feature of ENDOR spectra obtained using AM modulation is a background signal with an intensity that is inversely proportional to the RF frequency. The origin of this background signal lies in components of the RF field that are parallel to the magnetic field. These components produce a magnetic field modulation that desaturates the EPR signal and is thus measured as a background signal in the ENDOR spectrum.

The first thing of note is that the powder ENDOR signals are very weak. In our experience, this is typical of TM dopant complexes in AgCl, and it has limited the broader application of this technique in studies of photographic dispersions. The features at 1.19 MHz and 1.43 MHz are centred around the Larmor frequencies of ³⁷Cl and ³⁵Cl, respectively. These resonances result from chlorine matrix nuclei that are so far away from the dopant that their HF interaction is only composed of the electron–nuclear dipole–dipole contribution. The inset in figure 6 shows a precise scan of the region around 0.6 MHz. In addition to lines at the Larmor frequencies of ¹⁰⁹Ag (0.68 MHz) and ¹⁰⁷Ag (0.59 MHz), two pairs of lines appear around these matrix-ENDOR signals split by approximately 0.06 MHz. According to first-order perturbation theory, an isotropic HF interaction for the case of a paramagnetic defect with $S = \frac{1}{2}$ and $I = \frac{1}{2}$ leads to a pair of lines in the ENDOR spectrum. These lines are either split symmetrically about the
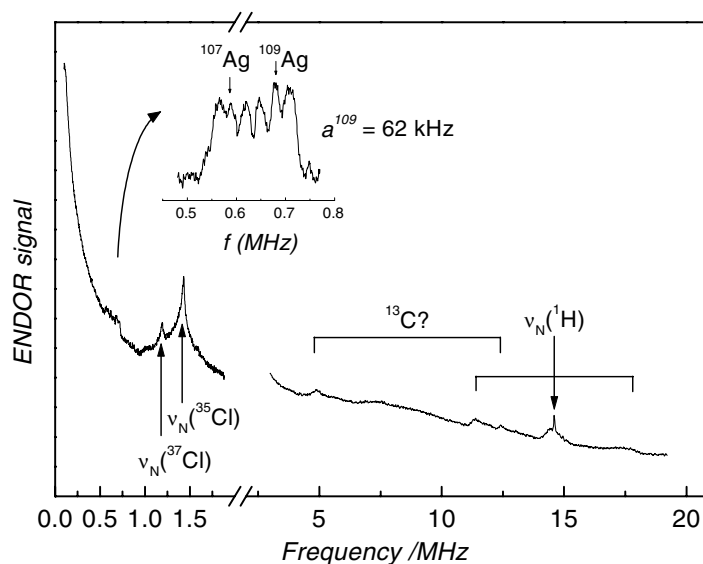
Figure 6. Powder ENDOR spectra obtained at 9 K and $B_0 = 342$ mT from a 0.35 μm cubic AgCl dispersion doped with 250 mppm [Cl$_5$Ir(NMP)]$^-$ following its exposure to 365 nm radiation. The expanded region shows a narrow scan around the Larmor frequencies of ^{107}Ag and ^{109}Ag. The assignment of the signals at 4.92 and 12.39 MHz to ^{13}C is speculative.

Larmor frequency ν_N by the frequency value of the hyperfine interaction W_{HF}/h, or they are split symmetrically about $W_{HF}/2h$ by $2\nu_N$. These two situations correspond to the conditions $\frac{1}{2}W_{HF} < \nu_N$ and $\frac{1}{2}W_{HF} > \nu_N$, respectively (Spaeth *et al* 1992). Since the pairs of lines in the inset of figure 6 are centred at the Larmor frequencies of ^{109}Ag and ^{107}Ag, they are attributed to HF interactions with silver nuclides for which $\frac{1}{2}W_{HF} < \nu_N$. On this basis, the measured HF interaction is 62 kHz for the ^{109}Ag isotope. There are also features at 4.92, 11.39, 12.39, 14.60 and 17.89 MHz in figure 6. 14.6 MHz corresponds to the Larmor frequency of ^{1}H at 342 mT. The lines at 11.39 MHz and 17.89 MHz are centred at this frequency. These lines could, therefore, come from interactions with hydrogen nuclei. For a purely isotropic interaction, their separation corresponds to the HF interaction, 6.5 MHz in this case. The lines at 4.92 MHz and 12.39 MHz are not centred on a Larmor frequency. Their separation, however, corresponds to about twice the Larmor frequency of ^{13}C. This situation would occur when the HF interaction is larger than the nuclear Zeeman (NZ) interaction. If the lines result from ^{13}C, the HF interaction is the sum of the two frequencies, i.e., 17.3 MHz. However, ^{13}C has a low natural abundance (1.11%), so that the detection of powder ENDOR signals from this nuclide would be surprising. For this reason, the lines at 4.92 MHz and 12.39 MHz cannot be assigned to carbon. An alternative explanation is that these lines are quadrupole transitions from a ^{14}N nucleus at a site with a large electric field gradient, but small electron density. However, experiments to be described next argue against such an interpretation.

An independent way to assign ENDOR lines to a specific nucleus is to measure their frequency dependences while varying the magnetic field. The B_0 field variation changes the NZ term in the spin Hamiltonian and, therefore, the variation in frequency is proportional to the nuclear g factor. In addition, for the case HF<NZ, both lines should shift in the same direction (to higher frequencies when the field is increased), whereas in the case HF>NZ they shift in opposite directions (with the low frequency line moving to lower frequency when the field is increased). Powder ENDOR spectra were obtained at magnetic field values ranging between

337.5 and 346.5 mT. For reasons of sensitivity, and in order to reduce the $1/f$ background signal, the spectra were measured using frequency modulation. The sign and magnitude of the shift of the ENDOR lines around 11.5 MHz and 18 MHz were consistent with an assignment to ^{1}H interactions. Both lines shifted upwards with increasing field by 43.1 ± 0.1 kHz mT^{-1}, corresponding to a nuclear g factor of 5.65 ± 0.04. This is very close to the ^{1}H nuclear g factor of 5.585 69. The line at 4.92 MHz shifted downward in frequency with increasing field consistent with the interpretation that it is the low field ENDOR line for the case $A/2 > g_N \mu_N B_0$. The shift was 17 ± 2 kHz mT^{-1} corresponding to a nuclear g factor of 2.2 ± 0.3. The nuclear g factors of ^{14}N and the magnetic isotopes of Cl, Ag and Ir all lie below 0.6. If the line were due to a ^{1}H interaction, it should have shifted upward with increasing field (since $A/2 < g_N \mu_N B_0$ in that case). Even with the large error estimated for the field-shift experiments, the nuclear g factor for ^{13}C ($= 1.4048$) also fails to correlate with this experimental result.

The ENDOR lines around the ^{1}H Larmor frequency were asymmetric, suggesting that this proton HF interaction is not isotropic. Since the anisotropy of the EPR line is small compared to the assumed EPR linewidth, the powder ENDOR spectrum will consist of signals corresponding to all orientations of the [Cl$_5$Ir(NMP)]$^{2-}$ complex with respect to B_0. Therefore, ENDOR lines caused by anisotropic interactions will manifest as 'powder-like' patterns. A reasonable correlation with the experimental data was achieved by simulating the shape of the ^{1}H ENDOR line assuming an anisotropic HF tensor (principal values $A_{XX} = 6.8 \pm 0.05$ MHz, $A_{YY} = 5.75 \pm 0.4$ MHz, $A_{ZZ} = 0 \pm 0.05$ MHz) and a random distribution of centres. The assignment of the principal values to the Cartesian axes is arbitrary. By contrast, satisfactory correlations could not be achieved assuming either isotropic or axial HF interactions. We assign these ^{1}H ENDOR lines to protons in the NMP ligand. The detection of proton ENDOR signals from the donor suggests the presence of an organic ligand in this centre, but the apparent absence of nitrogen ENDOR signals around the ^{14}N Larmor frequency, or resolved nitrogen HF splittings in the EPR spectrum, is surprising. The problem might be rooted in the anisotropic nature of the HF matrices expected for ^{14}N, i.e., they smear the powder ENDOR signals over wide frequency ranges in the region with a high $1/f$ background signal.

Figure 7 shows data obtained using a method whereby the overlapping EPR spectra of defects can be separated using non-overlapping ENDOR lines as a monitor. This ENDOR-induced EPR (EI-EPR) technique monitors the amplitude of a particular ENDOR line while scanning B_0. The frequency shift of the ENDOR lines due to the nuclear Zeeman interaction must be accounted for by a simultaneous sweep of B_0 and the ENDOR frequency (Niklas and Spaeth 1981). The upper figure shows the normal ENDOR spectrum measured at $B_0 = 342$ mT as a reference. The lower figure contains the EPR spectrum (trace a), the EI-EPR spectra measured at frequency positions indicated by arrows in the upper figure (traces b, c and d), and the EI-EPR spectra measured on the broad and narrow components of the ^{1}H matrix-ENDOR line (traces e and f). The EI-EPR spectra show that the lines at 4.9 MHz, 11.5 MHz and 18 MHz indeed belong to the EPR signal assigned to Ir˙ 4V. At $B_0 = 342$ mT, the shape of the ^{1}H matrix-ENDOR line is a superposition of a broad line ($\Delta f_{1/2} = 0.89$ MHz) and a narrow line ($\Delta f_{1/2} = 0.07$ MHz), both centred on the ^{1}H Larmor frequency. The EI-EPR spectra measured on the broad and narrow features (traces e and f) show that the narrow line belongs to the NMP complex, whereas the broad line comes from both the surface Ag^{2+} hole centre and the (gel)$^+$ radical.

As mentioned earlier, matrix-ENDOR lines result from nuclei at large distances from the paramagnetic centre so that their HF interactions are only composed of the electron–nuclear dipole–dipole interaction. In general, such matrix-ENDOR lines do not provide significant information about the defect's structure. However, if the defect is located at or near to the interface of two different materials (in this case, AgCl and gelatin), the detection
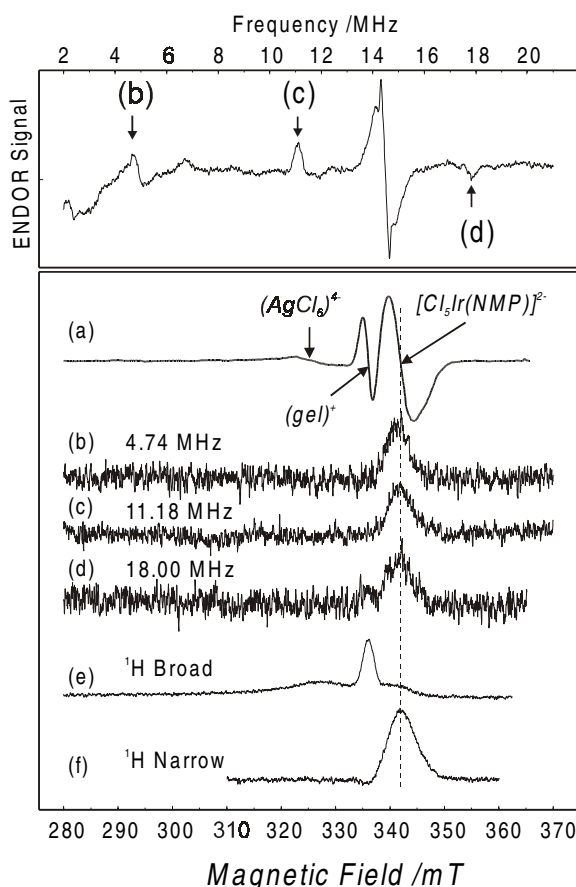
Figure 7. ENDOR-induced EPR spectra measured at 9 K from [Cl$_5$Ir(NMP)]$^-$-doped AgCl following 365 nm irradiation at 85 K. The upper figure shows the ENDOR spectrum measured at $B_0 = 342$ mT. EI-EPR spectra (b), (c) and (d) measured at frequency positions indicated by arrows in upper figure. EI-EPR spectra (e) and (f) measured on the broad and narrow components of the ^{1}H matrix-ENDOR lines.

of a matrix-ENDOR line from nuclides in the second matrix (gelatin) can give information about its proximity (in AgCl) to the interface region. The appearance of the ^{1}H matrix line in the ENDOR spectrum of the Ag^{2+} hole centre generated at 85 K is consistent with our conclusion that it is located near to, or on the surface of the AgCl grain. (We are discounting the possibility of interactions with water or gelatin peptizer occluded in the grain.) In this position, ^{1}H nuclei of residual gelatin or adsorbed water are sufficiently close to produce an ENDOR effect. Following the model of Hyde *et al* (1968) one can correlate the intensity and shape of 'distant' ENDOR lines to the distribution of matrix nuclei around the paramagnetic species. The electron–nuclear dipole–dipole interaction is proportional to r^{-3}, where r is the separation of the electron and the nucleus in a point-dipolar approximation. The magnitude of the ENDOR effect also depends on the electron–nuclear separation ($\sim r^{-6}$). In a continuum model, the matrix-ENDOR line shape is given by:

$$f(\nu) = \int_0^\pi \int_a^{(q/a)^{1/3}} \frac{\cos^2\varphi \sin^3\varphi}{r^4} \left[\frac{1}{\alpha^2 + (\nu - q/r^3)} + \frac{1}{\alpha^2 + (\nu + q/r^3)} \right] \, \mathrm{d}r \, \mathrm{d}\varphi$$

Table 3. ENDOR linewidths and distance parameters a calculated from the ^{1}H matrix-ENDOR lines of surface Ag^{2+}, the gelatin hole centre and $[Cl_5Ir(NMP)]^{2-}$.

Defect	Δf (FWHM) (MHz)	a^a (Å)
Surface Ag^{2+}	0.55	4.2
Gelatin hole centre	0.61	3.9
$[Cl_5Ir(NMP)]^{2-}$	0.07	8.0

[a] The lattice parameter for AgCl ≈ 5.55 Å.

where a defines the border between nuclei that are considered as bound to the paramagnetic defect ($r < a$) and those that are considered as matrix nuclei ($r > a$) and contribute only to the matrix-ENDOR line. The term in brackets constructs an individual Lorentzian shaped line with the linewidth α at the position given by the dipole–dipole interaction $q(\varphi)/r^3$ ($q(0) = 47.8$ MHz g_N, in atomic units). The upper limit of the integral marks the distance at which the dipole–dipole interaction becomes smaller than the width of an individual ENDOR line α, which, in the 'packet shifting' model of Feher (1959) is the limit for the ENDOR mechanism. α can sometimes be inferred from the narrowest ENDOR lines of 'bound' nuclei. It was chosen to be 80 kHz for the surface Ag^{2+} hole centre and the gelatin-related hole centre, and 8 kHz for the Ir· 4V. The simulated lineshapes were fitted to the experimental spectra from Ag^{2+}, the gelatin hole centre and Ir· 4V using a as the variable parameter. The best-fitted values of a are shown in table 3. The results for Ag^{2+} and Ir· 4V imply substantial populations of these defects reside within one to two unit cells from the grain's surface. This was even true for samples in which the dopant was nominally buried in a 0–40% band. Recent experience has shown that redistribution of the dopant during grain growth appears to be a common problem in the precipitation of AgX dispersions.

### 4.3. Spin population analyses and structural assignments

Atomic spin populations have been computed by the Hartree–Fock method for the $\{Ir· 4V\}^-$ trapped electron centre. Particular attention was given to the effects of vacancy association on the unpaired electron distribution. Table 4 includes data obtained for the seven most probable vacancy geometries of $\{Ir· 4V\}^-$. Of the three configurations with binding energies $\geqslant 5.0$ eV, $(101)(\bar{1}01)(011)(0\bar{1}1)$ is predicted to give substantial unpaired spin density on iridium. Such a high unpaired electron density would lead to resolved ${}^{191/193}$Ir HF splittings in EPR, as in the case of $(IrCl_6)^{4-}$ (Eachus and Graves 1976). These were not observed experimentally. This leaves the geometries $(101)(\bar{1}01)(01\bar{1})(0\bar{1}\bar{1})$ and $(101)(\bar{1}01)(110)(\bar{1}\bar{1}0)$ as possible alternatives. Because binding energy calculations predict the former is preferred by about 0.2 eV, the result of the slightly larger vacancy separations afforded by the $(01\bar{1})$ and $(0\bar{1}\bar{1})$ locations, we tentatively assign the $(101)(\bar{1}01)(01\bar{1})(0\bar{1}\bar{1})$ configuration to $\{Ir· 4V\}^-$.

The ^{1}H hyperfine splittings measured by ENDOR could originate from the backbone of the NMP ring or from its methyl substituent. In the former case, electron density at an α hydrogen nucleus originates primarily from spin polarization of the $>$C–H σ bond. By this mechanism, positive spin density on carbon will produce negative 1s electron density at the α hydrogen. The resultant HF splitting will be isotropic. An additional HF interaction resulting from a dipole–dipole mechanism can introduce an anisotropic contribution to the ^{1}H HF matrix. The ^{1}H HF matrix obtained by ENDOR can be analysed on the basis of this model if A_{yy} and A_{zz} are both negative. This leads to $A_{iso} = -4.18$, $B_{xx} = -2.62$, $B_{yy} = -1.57$ and $B_{zz} = 4.18$ MHz. A_{iso} can then be used to estimate ρ_k, the unpaired electron density on the adjacent carbon,

Table 4. Unpaired electron densities ($\times 10^3$) calculated by the Hartree–Fock method for several configurations of $\{Ir\cdot\ 4V\}^-$ in AgCl. (See scheme 1.)

Vacancy configuration	$\sum BE^a$ (eV)	Ir	$\sum Cl$	N_1	C_1	C_2	C_3	C_4	N_2	C_5
$(101)(\bar{1}01)(01\bar{1})(0\bar{1}\bar{1})$	5.2	1.54	0.69	661.75	82.41	79.30	57.32	57.87	51.34	0.41
$(101)(\bar{1}01)(013)(0\bar{1}3)$	4.7	898.63	90.53	8.93	0.48	0.48	0.25	0.26	0.04	0.02
$(101)(\bar{1}01)(011)(0\bar{1}1)$	5.2	887.91	112.05	0.03	0.00	0.00	0.00	0.00	0.00	0.00
$(10\bar{1})(\bar{1}0\bar{1})(01\bar{1})(0\bar{1}\bar{1})$	2.6	4.04	1.18	803.59	49.52	48.20	29.07	29.96	31.35	0.65
$(110)(\bar{1}\bar{1}0)(1\bar{1}0)(\bar{1}10)$	4.5	1.24	1.10	781.48	57.68	56.17	31.91	32.78	34.25	0.62
$(200)(\bar{2}00)(020)(0\bar{2}0)$	3.1	1.21	1.04	758.84	74.44	72.85	25.20	26.05	37.19	0.62
$(101)(\bar{1}01)(110)(\bar{1}\bar{1}0)$	5.0	1.28	0.66	655.26	84.00	80.76	58.66	59.18	52.20	0.41

[a] Total vacancy binding energies from table 1.
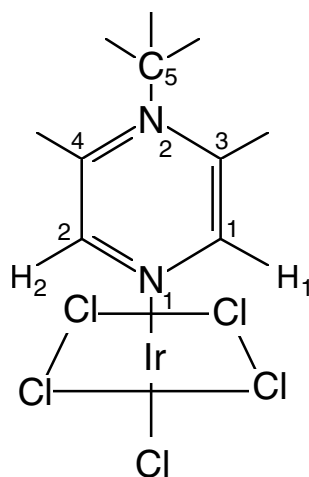
Scheme 1.

from the relationship:

$$\rho_k = A_{iso}/Q_k$$

where Q_k is an empirical constant with a value of about -70 MHz. Thus, ρ_k is approximately 0.06. This value is consistent with the Hartree–Fock unpaired electron densities calculated for carbons 1–4 in the $(101)(\bar{1}01)(01\bar{1})(0\bar{1}\bar{1})$ configuration (see table 4) and supports an assignment to a ring proton. Unfortunately, this is not an unambiguous interpretation since π electron density on N_2 could give substantial spin densities on the methyl protons via hyperconjugation. It is possible that the resultant β proton HF splittings are anisotropic and of the same magnitude as those from the ring protons.

Finally, the small silver HF splittings observed in ENDOR originate from those lattice cations closest to the atom with the largest unpaired electron density. According to calculation, these would be the Ag^+ ions located above and below the plane immediately adjacent to N_1 at positions (011) and $(0\bar{1}1)$ in figure 2. Assuming that the ^{109}Ag splitting of 62 kHz results entirely from population of an Ag 5s orbital, it corresponds to an unpaired electron density of about 3×10^{-5}.

5. Summary and conclusions

By combining X- and Q-band EPR and X-band ENDOR measurements with the results of atomistic and quantum mechanical calculations, an understanding of the effects of $[Cl_5Ir(NMP)]^-$ complexes on the photophysics of AgCl dispersions is emerging. There is indirect evidence from EPR and ENDOR experiments that $[Cl_5Ir(NMP)]^-$ is incorporated intact into AgCl by coprecipitation. Calculations show that a stable structure can be achieved when $[Cl_5Ir(NMP)]^-$ substitutes for an $(Ag_2Cl_7)^{5-}$ sub-unit of the host lattice. The NMP ring is rotated about 45° with respect to the equatorial chloride ligands, and the methyl ligand replaces Cl^-. Atomistic calculations show that the majority of these dopant centres will be charge compensated by association with four silver ion vacancies. A $(101)(\bar{1}01)(01\bar{1})(0\bar{1}\bar{1})$ geometry is slightly favoured for Ir 4V, where the Cl–Ir–(NMP) axis defines z. The computed vacancy binding energies are sufficiently large that, in grains with edge lengths $\geqslant 0.05$ μm, neutral Ir 4V centres should predominate between 10 and 298 K. The results of photo-EPR experiments suggest that there is also a small population of under-compensated Ir 3V centres in many of the dispersions studied.

Doping AgCl dispersions with $[Cl_5Ir(NMP)]^-$ extends their optical sensitivity out to about 440 nm at 10 K. During exposures to actinic light, this dopant traps electrons. Since its LUMO is primarily a π^* NMP orbital, the initial photoproducts are ligand-centred, one-electron donors. These have been tentatively identified as Ir˙ 4V and Ir˙ 3V from a combination of X- and Q-band EPR data and theoretical results. Powder ENDOR data have been obtained for Ir˙ 4V. In the absence of $^{191/193}$Ir HF and $^{35/37}$Cl or ^{14}N SHF data, structural assignments have been based on (i) the results of calculations of structure and energy, (ii) the detection of ^{1}H signals by ENDOR for Ir˙ 4V and (iii) the experimental g matrices. The ^{1}H HF data assigned to Ir˙ 4V are also consistent with the unpaired electron distribution calculated by Hartree–Fock methods for the favoured $(101)(\bar{1}01)(01\bar{1})(0\bar{1}\bar{1})$ geometry, *if* polarization effects from the bound vacancies are taken into account. {Ir˙ 4V}⁻ is thermally ionized before it can relax to {Ir˙ 3V}⁰, so that the photographic effects attributed to $[Cl_5Ir(NMP)]^-$ doping of AgCl dispersions (Olm *et al* 1994) must be attributed to the kinetic properties of the overcompensated centre.

Acknowledgments

Appendix

In this section, we present some details of the various calculations performed on the $[Cl_5Ir(NMP)]^{n-}$ dopant embedded in the AgCl lattice. The atomistic calculation is considered first. The short range functions between this dopant and the crystal ions were of the Buckingham form and are given in table A1. The dopant ions were considered to be non-polarizable and interacted with the shells of crystal ions. The corresponding short range interactions between the polarizable crystal ions are well known (Catlow *et al* 1987). In the course of this work we attempted to develop intramolecular potential functions for the dopant that would allow full geometric optimization in the atomistic calculation. This goal was not achieved, and so the geometry was fixed at the positions determined quantum mechanically.

The quantum mechanical calculations were performed at the Hartree–Fock level. The dopant was treated within a neutral, spherical point-ion array with appropriate ions removed for spatial considerations. For $[Cl_5Ir(NMP)]^{n-}$, this required the removal of $(AgCl_6AgCl)$, where

Table A1. Buckingham short range functions $V(r) = A\,e^{-r/\rho} - C/r^6$.

Interaction	A (eV)	r (Å)	C (eV Å^6)
Ag$^+$–Ir	6737.1	0.262 59	0.0
Cl$^-$–Ir	2562.9	0.289 97	0.0
Ag$^+$–H	1943.0	0.211 84	14.5
Cl$^-$–H	2282.4	0.228 68	0.0
Ag$^+$–Cl	211.2	0.433 22	0.0
Cl$^-$–Cl	1227.2	0.321 40	75.0
Ag$^+$–C	617.4	0.293 77	0.0
Cl$^-$–C	249.3	0.318 84	0.0
Ag$^+$–N	715.1	0.292 54	0.0
Cl$^-$–N	288.4	0.318 84	0.0

the first silver ion is centred at the origin. Vacancies near the dopant were then simulated by removal of other point ions. The point ions representing Ag$^+$ adjacent to the dopant contained a Born–Mayer function:

$$V(r) = A\,e^{-\alpha r}$$
$$A = 715.06\ \text{eV}$$
$$\alpha = 0.278\,69\ \text{Å}$$

which simulated short range interactions between the dopant and crystal ions. The geometry of the dopant was fully optimized with the CADPAC programme (Amos *et al* 1995), where the total energy including short range interactions was computed. This procedure was applied to each dopant–vacancy configuration. The basis sets employed were at the double-zeta level contained within the programme.

References

Amos R D *et al* 1995 *The Cambridge Analytic Derivatives Package* Issue 6
Baetzold R C 1997 *J. Phys. Chem.* B **101** 1130
——2000 to be published
Bell E L, Reed K J and Olm M T 1992 *US Patent* 5 132 203
Bennebroek M T, Arnold A, Poluektov O G, Baranov P G and Schmidt J 1996 *Phys. Rev.* B **54** 11 276
Bennebroek M T, Poluektov O G, Zakrzewski A J, Baranov P G and Schmidt J 1995 *Phys. Rev. Lett.* **74** 442
Berry C R 1977 *The Theory of the Photographic Process* ed T H James (New York: Macmillan) ch 3
Catlow C R A, Corish J, Harding J H and Jacobs P W M 1987 *Phil. Mag.* **55** 481
Eachus R S and Graves R E 1974 *J. Chem. Phys.* **61** 2860
——1976 *J. Chem. Phys.* **65** 1530
Eachus R S, Graves R E and Olm M T 1978 *Phys. Status Solidi* **88** 705
Eachus R S and Olm M T 1986 *Annu. Rep. Prog. Chem.* C **83** 3
——1991 *J. Soc. Photogr. Sci. Technol. Japan* **54** 294
Eachus R S, Pawlik Th D, Baetzold R C, Poluektov O and Schmidt J 1999 *Phys. Rev.* B **59** 8560
Endo K and Saikawa M 1990 *J. Photogr. Sci.* **38** 210
Feher G 1959 *Phys. Rev.* **114** 1219
Gale J D 1997 *J. Chem Soc. Faraday Trans.* **93** 629
Höhne M and Stasiw M 1968a *Phys. Status Solidi* **25** K55
——1968b *Phys. Status Solidi* **28** 247
Hyde J S, Rist G H and Erikson L E 1968 *J. Phys. Chem.* **72** 4269
Marchetti A P and Eachus R S 1992 *Advances in Photochemistry* vol 17, ed D Volman, G Hammond and D Neckers (New York: Wiley) pp 145–216
McGavin D G, Mombourquette M J and Weil J A 1993 *Computer program EPR-FOR* version 5.1, Department of Chemistry, University of Saskatchewan

Moser F and Ahrenkiel R K 1977 *The Theory of the Photographic Process* ed T H James (New York: Macmillan) ch I
Niklas J R and Spaeth J-M 1981 *Phys. Status Solidi* b **101** 221
Olm M T, McDugle W G, Puckett S A, Kuromoto T Y, Eachus R S, Bell E L and Wilson R D 1994 *US Patent* 5 360 719
Olm M T and Eachus R S 1999 *Radiat. Eff. Defects Solids* **150** 71
Paul W B, Goldenberg S, Rowan L and Slifkin L 1987 *Cryst. Latt. Defects Amorph. Mater.* **15** 197
Spaeth J-M, Niklas J R and Bartram R H 1992 *Structural Analysis of Point Defects in Solids* (Berlin: Springer)
Toma H E and Mailin J M 1973 *Inorg. Chem.* **12** 1039